(*30*–*32*), and the dissociated hydrogen (denoted as H* in Fig. 1) appearing on the surface of the opposite side of the membrane immediately reacts with oxygen to give HOO· and H_2O_2. Then H_2O_2 is decomposed to HO·, atomic oxygen, and water. In the direct hydroxylation (*8*–*12*) of hydrocarbons with oxygen and hydrogen catalyzed by transition metals, it has been considered so far that, at the first step, oxygen and hydrogen react with the catalysis of the metals to give hydrogen peroxide. We also recognized that this membrane reactor can easily produce hydrogen peroxide under the reaction conditions used here without hydrocarbons, and quite recently it was reported (*33*) that a similar palladium membrane works well in water as a reactor for the direct production of hydrogen peroxide from oxygen and hydrogen. Oxene, one of the active oxygen species produced by the decomposition of hydrogen peroxide, has been known to easily add to carbon-carbon double bonds, including conjugated ones such as benzene (*7*, *34*). This type of addition is 10^3 times faster in rate than the hydrogen abstraction from the methyl group (*7*, *35*). Thus, it is not unreasonable to consider that oxene is largely responsible for the hydroxylation in this membrane process.

If the HO· radical is the main active species, as has been considered (*12*), benzyl alcohol and benzaldehyde should be produced more in the hydroxylation of toluene, as occurs with EuX_3-$TiO(acac)_2$-Pt oxide/SiO_2 (X = Cl and ClO_4) catalysts (*15*). However, it is difficult to specify the real active species from the three (HOO·, HO·, and oxene) at present, although it seems likely that the active oxygen species is derived from HOO· and H_2O_2.

It should be emphasized that this membrane system could be practical, because it is simple in structure; produces phenol in a yield of 1.5 kg per kilogram of catalyst per hour; and has a low probability of causing a detonating gas reaction, because oxygen and hydrogen are not simultaneously mixed.

References and Notes

1. For example, at the first step for the production of cumene from benzene and propylene with the traditional supported phosphoric acid catalyst (200° to 250°C, 14 to 21 kg/cm^2), the benzene conversion is about 20%, and at the second step for the oxidation of cumene to cumene hydroperoxide with air (80° to 130°C), the conversion is about 25%. At the third step for the decomposition of cumene hydroperoxide to phenol and acetone with sulfuric acid, phenol is produced in a yield over 93%. Accordingly, in this traditional process, the one-pass yield of phenol based on the amount of benzene initially used is less than 5%.
2. G. I. Panov, *CATTECH* **4**, 18 (2000).
3. G. Bellussi, C. Perego, *CATTECH* **4**, 4 (2000).
4. P. P. Notté, *Topics Catal.* **13**, 387 (2000).
5. N_2O is the main component of the NO_x emitted during the oxidation of cyclohexanol and cyclohexanone to adipic acid with nitric acid. However, unless such N_2O is available, it has to be obtained by the oxidation of ammonia produced from nitrogen and hydrogen and is expensive.
6. M. G. Clerici, P. Ingallina, *Catal. Today* **41**, 351 (1998).
7. Y. Moro-oka, M. Akita, *Catal. Today* **41**, 327 (1998).
8. A. Kunai, K. Ishihata, S. Ito, K. Sasaki, *Chem. Lett.* 1967 (1988).
9. A. Kunai, *et al.*, *Catal. Lett.* **4**, 139 (1990).
10. T. Kitano, *et al.*, *J. Chem. Soc. Perkin Trans. 2*, **1990**, 1991 (1990).
11. T. Tatsumi, K. Yuasa, H. Tominaga, *J. Chem. Soc. Chem. Commun.* **1992**, 1446 (1992).
12. T. Miyake, M. Hamada, Y. Sasaki, M. Oguri, *Appl. Catal. A Gen.* **131**, 33 (1995).
13. K. Otsuka, I. Yamanaka, K. Hosokawa, *Nature* **345**, 697 (1990).
14. I. Yamanaka, K. Nakagaki, T. Akimoto, K. Otsuka, *J. Chem. Soc. Perkin Trans.* **2**, 2511 (1996)
15. I. Yamanaka, T. Nabeta, S. Takenaka, K. Otsuka, *Stud. Surf. Sci. Catal.* **130**, 815 (2000).
16. K. Otsuka, I. Yamanaka, *Catal. Today,* **57**, 71 (2000).
17. T. Jintoku, H. Taniguchi, Y. Fujiwara, *Chem. Lett.* **1987**, 1865 (1987).
18. T. Jintoku, K. Nishimura, K. Takaki, Y. Fujiwara, *Chem. Lett.* **1990**, 1687 (1990).
19. L. C. Passoni, A. T. Cruz, R. Buffon, U. Schuchardt, *J. Mol. Catal. A Chem.* **120**, 117 (1997).
20. I. Yamanaka, M. Katagiri, S. Takenaka, K. Otsuka, *Stud. Surf. Sci. Catal.* **130**, 809 (2000).
21. B. Liptáková, M. Hronec, Z. Cvengrošová, *Catal. Today* **61**, 143 (2000).
22. A. Thangaraj, R. Kumar, P. Ratnasamy, *Appl. Catal.* **57**, L1 (1990).
23. C. W. Lee, W. J. Lee, Y. K. Park, S.-E. Park, *Catal. Today*, **61**, 137 (2000).
24. D. Bianchi, *et al.*, *Angew. Chem. Int. Ed.* **39**, 4321 (2000).
25. The phenol yields based on the amount of benzene initially used are 2.79% for the hydroxylation with oxygen and carbon monoxide (*17*, *18*), 3.4 to 4.3% for the hydroxylation with oxygen (*20*, *21*), and 0.085 to 18.15% for the hydroxylation with expensive hydrogen peroxide (*11*, *22*–*24*).
26. S. Yan, H. Maeda, K. Kusakabe, S. Morooka, *Ind. Eng. Chem. Res.* **33**, 616 (1994).
27. This means that the reaction of oxygen with dissociated hydrogen permeating through the membrane is faster than the recombination between the dissociated hydrogen atoms themselves on the opposite membrane surface. At the same time, this suggests that under our reaction conditions, the rate-limiting step for the conversion of benzene to phenol is the reaction between oxygen and hydrogen rather than the hydrogen permeation, and direct mixing of oxygen and hydrogen in gas phase is very limited (oxygen and hydrogen are well separated except on the membrane interface where both meet).
28. The ratios of water to phenol were changed with the palladium membranes used, because it is impossible to prepare exactly the same membranes. Generally speaking, the ratios were lower with the membranes that showed higher performance for the phenol formation.
29. The deterioration was mainly due to peeling off of the palladium thin layer from the α-alumina tube. This peeling off could be suppressed by coating the thin layer with a certain polymer. The polymer-coated membrane also works well for the hydroxylation.
30. B. J. Wood, H. Wise, *J. Catal.* **5**, 135 (1966).
31. V. M. Gryaznov, M. G. Slin'ko, *Faraday Discuss. Chem. Soc.* **72**, 73 (1981)
32. N. Itoh, W.-C. Xu, *Appl. Catal. A Gen.* **107**, 83 (1993).
33. V. R. Choudhary, A. G. Gaikwad, S. D. Sansare, *Angew. Chem. Int. Ed.* **40**, 1776 (2001).
34. S. Sato, R. J. Cvetanović, *J. Am. Chem. Soc.* **81**, 3223 (1959).
35. M. G. Neumann, N. Jonathan, *J. Chem. Soc. B* **1970**, 167 (1970).

36. We thank the New Energy and Industrial Technology Development Organization (NEDO) for financial support.

24 September 2001; accepted 14 November 2001

Constraints on Melt Movement Beneath the East Pacific Rise From ^{230}Th-^{238}U Disequilibrium

Haibo Zou,[1,2]* Alan Zindler,[2] Yaoling Niu[3]

We report ^{230}Th-^{238}U disequilibrium data on mid-ocean ridge basalts recovered 5 to 40 kilometers off the ridge axis near 9°30′N of the East Pacific Rise. These data indicate near-symmetrical eruptions of normal mid-ocean ridge basalts (NMORBs) and incompatible element–enriched mid-ocean ridge basalts (EMORBs) as far as 20 kilometers off axis. Our results suggest large-scale subsurface lateral transport of NMORB melt at 19 to 21 centimeters per year and also provide constraints on the petrogenesis of EMORBs of off-axis origin.

Lavas that erupt on the seafloor away from the axis of mid-ocean ridges (MORs) contain information about melting, melt movement, and crustal accretion processes associated with MOR spreading centers (*1*–*3*). For off-axis basalts to be used to develop a better understanding of the process of melt movement, they must be demonstrably distinguished from those originally erupted at the ridge axis. ^{230}Th-^{238}U disequilibrium can provide temporal information crucial to identifying basalts of off-axis origin and has been used to study basalts as far as 4 km away from the ridge axis (*4*). To span a scale of melt movement beneath MORs that may be greater than 4 km, and to avoid large axial eruptions that send lava flows as far as 3.5 km away from the axis (*5*), we measured the ^{230}Th-^{238}U disequilibrium of basalts from 5 to 40 km off-axis.

Our samples were collected during the

[1]Department of Earth and Space Sciences, University of California at Los Angeles, Los Angeles, CA 90095, USA. [2]National High Magnetic Field Laboratory and Department of Geological Sciences, Florida State University, Tallahassee, FL 32306, USA. [3]Department of Earth Sciences, Cardiff University, Cardiff, CF10 3YE, UK.

*To whom correspondence should be addressed. E-mail: hzou@ess.ucla.edu

Phoenix-02 cruise (research vessel *Melville*) by dredging out to 40 to 50 km from the East Pacific Rise (EPR) on both the Cocos and Pacific plates near 9°30′N. In the vicinity of 9°30′N, the EPR spreads almost symmetrically at 11.1 cm year^{-1} (*6*). Therefore, basalt sampled at distances of 40 to 50 km from the ridge axis corresponds to a spreading age of about 800 thousand years ago (ka). Samples were analyzed by secondary ion mass spectrometry for Th isotopes and thermal ionization mass spectrometry for U and Pb isotopes (*7*). Pb isotopic compositions exhibited small variations in $^{208}Pb/^{204}Pb$ (37.60 to 38.05), $^{207}Pb/^{204}Pb$ (15.47 to 15.57), and $^{206}Pb/^{204}Pb$ (18.18 to 18.56) ratios (Table 1). Because these Pb isotopic compositions represent long-term source U/Pb and Th/Pb ratios, the small range in Pb isotopic compositions for these basalts suggests a long-term, relatively homogeneous, U/Pb and Th/Pb source. ($^{234}U/^{238}U$) ratios (where parentheses indicate an activity ratio) of all samples are close to 1.0, indicating that the Th-U systematics has not been perturbed by post-eruption alteration. The ($^{230}Th/^{238}U$) ratios of the off-axis basalts are therefore controlled by their initial (at the time of eruption) ($^{230}Th/^{238}U$) ratios and by the time elapsed since the eruption. The initial ($^{230}Th/^{238}U$) ratios are determined by the mineralogy of the source of the melt (such as the relative amount of garnet and clinopyroxene) and the melting processes (such as the rate of melting and the porosity of the melting zone) (*8*–*11*). The initial ($^{230}Th/^{238}U$) ratios are independent of the source ($^{230}Th/^{238}U$) ratios because the source, before melting, is assumed to have reached secular equilibrium, or ($^{230}Th/^{238}U$) = 1.

Our samples show almost symmetrical patterns of ($^{230}Th/^{238}U$) variation with distance from the axis (Fig. 1A), which are consistent with the symmetric patterns of K/Ti (Fig. 1B) and MgO (*12*) variations about the axis (*13*). Extending out to about 16 km on either side of the ridge axis at 9°30′N, ($^{230}Th/^{238}U$) ratios decrease from 1.158 to 1.233 [the range of zero-age samples from Goldstein *et al*. (*14*)] to 1.036 (sample PH6-2). This decrease can be explained by the aging of the seafloor away from the spreading axis (Fig. 1), assuming that the basalts had a similar range in initial ($^{230}Th/^{238}U$) of 1.158 to 1.233. Farther away from the axis, there are changes in ($^{230}Th/^{238}U$) ratios. On the Cocos plate, the ($^{230}Th/^{238}U$) ratios increase to 1.130 (PH8-1) and then drop to 0.894 (PH10-2), and on the Pacific plate, the ($^{230}Th/^{238}U$) ratios increase to 1.084 (PH33-3) and then decrease to 0.849 (PH34-1). Sam-

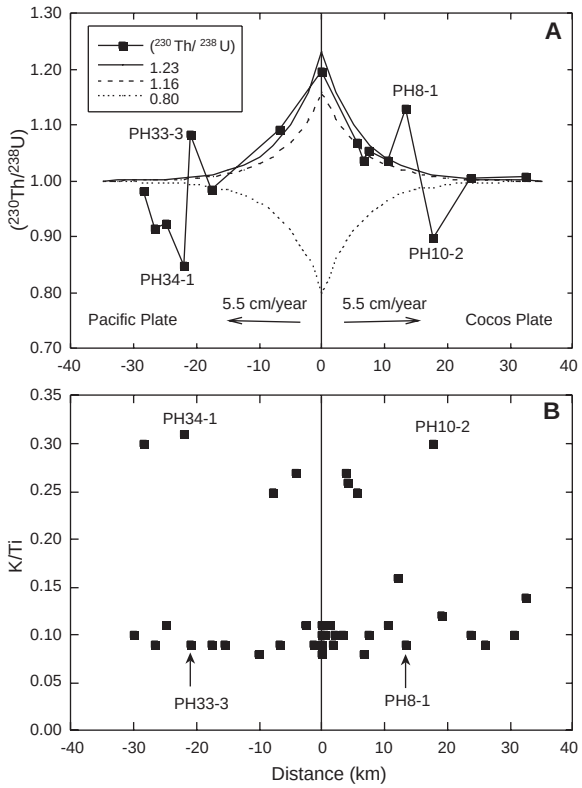

Fig. 1. (**A**) Comparison of three measured ($^{230}Th/^{238}U$) ratios with calculated ($^{230}Th/^{238}U$) ratios using a half-spreading rate of 5.5 cm year^{-1} and initial ($^{230}Th/^{238}U$) ratios right after eruption of 1.23, 1.16, and 0.80, respectively. (**B**) Plot of K/Ti versus distance from the axis. Near axis (<4 km) data are from (*35*).

Table 1. Locations of the basaltic samples at EPR 9°30′N and their U-Th disequilibrium and Pb isotope data. Distances from the ridge axis have uncertainties of less than 0.5 km. Measurement errors (2σ) in U and Th concentrations by isotope dilution are <0.5%. The errors (2σ) range from 0.5 to 0.8% for ($^{238}U/^{232}Th$) and from 0.6 to 1.2% for ($^{230}Th/^{238}U$). Decay constants: $\lambda^{238} = 1.55125 \times 10^{-10}$ year^{-1}, $\lambda^{234} = 2.8262 \times 10^{-6}$ year^{-1}, $\lambda^{230} = 9.195 \times 10^{-6}$ year^{-1}, and $\lambda^{232} = 4.948 \times 10^{-11}$ year^{-1}. P10-2R and P37-1R are duplicate samples for Th concentration and ($^{230}Th/^{232}Th$) only. U concentrations from P10-2 and P37-1 are used to calculate ($^{238}U/^{232}Th$) and ($^{230}Th/^{238}U$) for P10-2R and P37-1R, respectively. ppb, parts per billion.

Sample	Latitude (N)	Longitude (W)	Depth (m)	Distance (km)	U (ppb)	Th (ppb)	($^{234}U/^{238}U$)	($^{238}U/^{232}Th$)	($^{230}Th/^{232}Th$)	($^{230}Th/^{238}U$)	$^{208}Pb/^{204}Pb$	$^{207}Pb/^{204}Pb$	$^{206}Pb/^{204}Pb$
P2-3	9°31.05′	104°11.29′	2888	5.7	259	751	1.006 ± 9	1.046	1.119 ± 7	1.070	37.984	15.542	18.534
P3-1	9°31.10′	104°10.76′	2771	6.7	48	117	1.008 ± 11	1.234	1.280 ± 9	1.037	37.771	15.510	18.248
P4-1	9°31.19′	104°10.34′	3018	7.4	70	170	1.011 ± 16	1.244	1.313 ± 11	1.055	37.777	15.490	18.326
P6-2	9°31.44′	104°08.60′	2980	10.6	65	164	1.011 ± 8	1.203	1.246 ± 8	1.036	37.817	15.496	18.360
P8-1	9°31.50′	104°07.75′	2963	13.3	59	138	1.025 ± 13	1.296	1.464 ± 11	1.130	37.807	15.495	18.365
P10-2	9°31.87′	104°04.71′	3123	17.7	230	444	1.009 ± 9	1.573	1.407 ± 13	0.894	37.603	15.493	18.184
P10-2R	9°31.87′	104°04.71′	3123	17.7		446		1.567	1.407 ± 17	0.898			
P14-1	9°31.99′	104°01.55′	2880	23.5	39	93	1.006 ± 11	1.264	1.270 ± 10	1.005	38.051	15.569	18.513
P18-2	9°31.46′	103°56.67′	3080	32.4	127	330	1.006 ± 9	1.163	1.174 ± 10	1.009	37.732	15.493	18.274
P23-1	9°30.45′	104°18.09′	2627	−6.7	57	96	1.014 ± 5	1.793	1.960 ± 20	1.093	37.777	15.499	18.286
P31-9	9°29.87′	104°23.97′	2891	−17.7	70	165	1.010 ± 4	1.294	1.274 ± 10	0.984	37.620	15.467	18.187
P33-3	9°29.35′	104°25.72′	2920	−21.0	65	146	1.014 ± 5	1.344	1.457 ± 10	1.084	37.712	15.484	18.242
P34-1	9°29.29′	104°26.27′	2800	−22.0	255	622	1.006 ± 5	1.243	1.055 ± 7	0.849	37.791	15.513	18.361
P35-1	9°29.21′	104°27.79′	2971	−24.7	105	235	1.009 ± 5	1.352	1.248 ± 15	0.923	37.673	15.474	18.227
P36-7	9°29.20′	104°28.90′	2787	−26.7	50	109	1.013 ± 8	1.402	1.284 ± 10	0.916	37.710	15.479	18.270
P37-1	9°29.04′	104°29.78′	2857	−28.4	251	742	1.012 ± 5	1.026	1.004 ± 8	0.982	38.024	15.521	18.556
P37-1R	9°29.04′	104°29.78′	2857	−28.4		733		1.038	1.019 ± 8	0.988			

ples PH8-1 and PH33-3, with ^{230}Th excesses, have almost identical light rare earth element (LREE)–depleted patterns, and both are normal mid-ocean ridge basalts (NMORBs); samples PH10-2 and PH34-1, however, with ^{230}Th deficits, have similar LREE-enriched patterns, and both are incompatible element–enriched mid-ocean ridge basalts (EMORBs) (Fig. 2). Assuming that PH33-3 was initially erupted at the axis and then moved to its present position by seafloor spreading, and using a half-spreading rate of 5.5 cm year^{-1} (*6*), the age predicted from its location would be about 350 ka (about five half-lives of ^{230}Th). Given the highest zero-age (^{230}Th/^{238}U) ratio of 1.233 as the initial value, secular equilibrium should have been achieved in PH33-3 after 350 ka. Similarly, using the same spreading rate and initial (^{230}Th/^{238}U) ratio, the predicted (^{230}Th/^{238}U) ratio would be 1.017 for PH8-1. From a different perspective, if we again assume both PH33-3 and PH8-1 were erupted on axis, then the initial (^{230}Th/^{238}U) ratios for these two NMORBs would have been about 3.0. However, (^{230}Th/^{238}U) ratios reported so far for zero-age MORBs globally are less than 1.5 (*15*). We suggest that samples PH8-1 and PH33-3 were formed by off-axis volcanism by melting of a source with $D_{Th} < D_U$, where D_{Th} and D_U are bulk partition coefficients for Th and U, respectively (*16*). One candidate source may be peridotites with garnet and/or high-sodium clinopyroxenes (*17–20*) from the upper mantle. The two EMORB samples (PH10-2 and PH34-1) that have (^{230}Th/^{238}U) ratios of less than 1.0 are even farther away from the spreading ridge and should not have any detectable U-Th disequilibrium if they were originally erupted at the axis. Therefore, they were also produced by off-axis volcanism. Because their (^{230}Th/^{238}U) ratios are as far from secular equilibrium as those measured from samples from the mid-Atlantic ridge at 29° to 30°N (*15*), we infer that they erupted close to their present locations. Unlike samples PH8-1 and PH33-3, with (^{230}Th/^{238}U) ratios greater than 1.0, samples PH10-2 and PH34-1, with (^{230}Th/^{238}U) ratios less than 1.0, were principally produced by melting in a source with $D_{Th} > D_U$. One candidate source is a calcium-clinopyroxene–rich spinel peridotite from the upper mantle (*21–24*). Samples PH35-1 and PH36-7 on the Pacific plate also have (^{230}Th/^{238}U) ratios less than 1.0, but their (^{230}Th/^{238}U) ratios are somewhat closer to secular equilibrium than is that of PH34-1, which is consistent with the fact that they are farther away from the spreading axis. As for samples PH14-1, PH18-2, and PH37-1, which are also well off axis, their (^{230}Th/^{238}U) ratios are close to 1.0. Their close approach to secular equilibrium indicates that they are >350 ka. Consequently, these three samples were most likely produced at the ridge axis. Samples PH19-4 (at +39.8 km) and PH39-2 (at –31.9 km), farthest away from the ridge axis, were also erupted at the ridge axis, based on ^{40}Ar-^{39}Ar ages of >500 ka for both samples (*25*).

Based on estimated initial (^{230}Th/^{232}Th) and (^{231}Pa/^{235}U) ratios in MOR samples collected 4 km from the ridge axis, Goldstein *et al*. (*4*) inferred that some volcanism can occur as far as 4 km away from the spreading axis. Our U-Th disequilibrium study of basalts recovered from as far as 40 km away from the axis supports the occurrence of off-axis eruptions and further suggests that some volcanism can occur at more than 20 km off axis. More importantly, our results place constraints on melt movement beneath MORs. Off-axis vents could have erupted either lavas transported laterally from a focused axial magma system or those transported vertically from independent off-axis magma systems. Although symmetric off-axis NMORB magma systems cannot be ruled out, the fact that PH8-1 and PH33-3 have similar trace element compositions (Fig. 2) can be explained by subsurface lateral transport of magma from the same axial system in opposite directions (Fig. 3). The physics for the large-scale subsurface lateral transport of melt is not clear. A possible mechanism is continued sill propagation under the condition of sufficient magma supply (*26*). Based on our model (*27*), the lateral velocity of the melt that generated basalts PH8-1 and PH33-3 is calculated to be 19 to 21 cm year^{-1}, which is much faster than the half-spreading rate of 5.5 cm year^{-1}. On the other hand, off-axis eruptions of EMORB samples such as PH10-2 and PH34-1 can be explained by independent symmetric off-axis magma systems, because EMORBs with ^{238}U excesses have not been reported among measured zero-age ridge axis basalts at 9°30′N (*14*). The enrichments in LREEs and the low (^{230}Th/^{238}U) ratios in PH10-2 and PH34-1 are consistent with a metasomatized spinel peridotite source that contains calcium-clinopyroxene and amphibole. Similarity among the Pb isotopic compositions of these basalts and of other NMORBs suggests that the mantle source was not metasomatized long enough ago to change Pb isotopic compositions. The observed peaks at Nb and Ta in the primitive mantle–normalized spider diagram (*28*, *29*) in these two samples (Fig. 2) suggest that a likely source of the metasomatic fluids is recycled oceanic crust (*30–32*). The proximity of lavas with high (^{230}Th/^{238}U) > 1.0

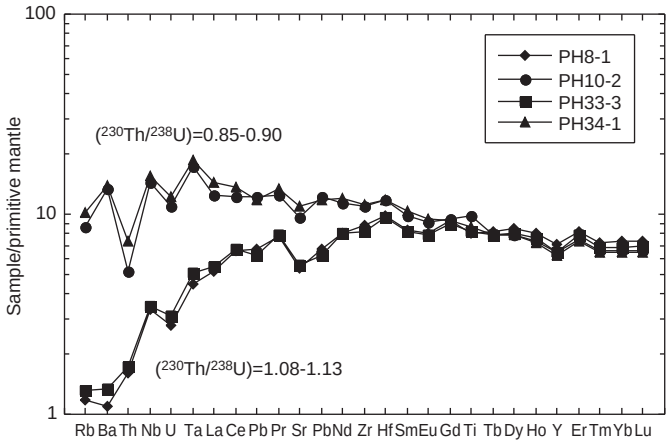

Fig. 2. Primitive mantle–normalized abundance patterns for highly to moderately incompatible elements in four samples with unusual U-Th disequilibrium results. Normalizing values are from (*29*).

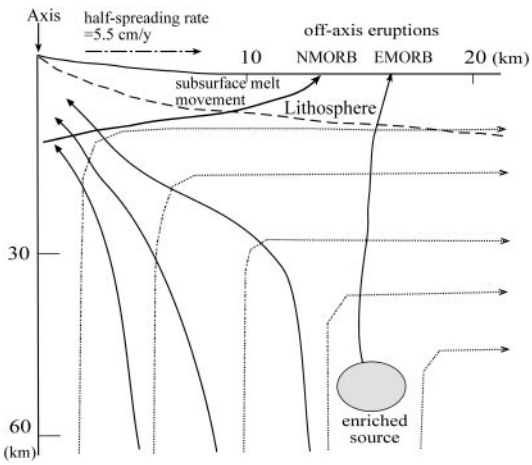

Fig. 3. A sketch illustrating the mantle dynamics beneath the MOR at 9°30′N constrained by U-Th disequilibrium data. The sketch shows only the right half of the near-symmetrical melting zone. Dotted lines represent solid mantle flow, solid lines represent melt flow, and the dashed line is the base of lithosphere. The enriched mantle blob may not be restricted to the marked region.

(e.g., PH33-3) and those with low (^{230}Th/^{238}U) < 1.0 (e.g., PH34-1) suggests spatially restricted magma transport routes to the surface for some off-axis volcanism. In addition, near-symmetrical off-axis eruptions in a broad region are more consistent with passive mantle flow driven by plate motion (*1*, *2*) than with active mantle flow driven by buoyancy in a narrow region (about a few kilometers).

References and Notes

1. D. W. Forsyth *et al*., *Science* **280**, 1215 (1998).
2. M. Spiegelman, J. R. Reynolds, *Nature* **402**, 282 (1999).
3. J. R. Reynolds, C. H. Langmuir, *G*^{3} **1**, 1999GC000033 (2000).
4. S. J. Goldstein, M. R. Perfit, R. Batiza, D. J. Fornari, M. T. Murrell, *Nature* **367**, 157 (1994).
5. P. Gente, J. M. Auzende, V. Renard, Y. Fouquet, D. Bidean, *Earth Planet. Sci. Lett.* **78**, 224 (1986).
6. S. Carbotte, K. Macdonald, *J. Geophys. Res.* **97**, 6959 (1992).
7. Glass chips (<500 μm) were carefully picked under a binocular microscope to avoid oxides or alteration coatings, ultrasonically cleaned, and then ground by hand in an agate mortar. Picked glass was then leached in a 1:1 mixture of 30% H_2O_2 and 2.5 M HCl for 10 min at room temperature to efficiently dissolve and remove Mn oxides without affecting Th/U ratios. Samples for U-Th isotope analyses were spiked with a ^{233}U-^{229}Th spike and dissolved in a HF-$HClO_4$–HCl-HNO_3 mix, and samples for Pb isotope analyses were dissolved in a HF-HBr mix. Th isotopes were measured by ISOLAB 54, and U and Pb isotopes were measured by MAT 262 RPQII. Chemically purified Th was loaded with colloidal graphite onto a pyrolitically coated graphite rod and ionized with a primary Ar^+ ion beam. This technique yields high Th ionization efficiencies (0.5 to 2%). Repeat analyses of a Th standard solution WUN-1 yielded a mean of $4.297 \pm 0.045 \times 10^{-6}$ (2σ) for (^{230}Th/^{232}Th) atomic ratios. U, loaded with colloidal graphite, was ionized on a single Re filament, and the (^{235}U/^{238}U) ratio was used to correct for mass fractionation. Pb samples were loaded with concentrated silica gel onto single Re filaments. Pb isotope data were corrected for fractionation of 0.13% per atomic mass unit for ^{206}Pb/^{204}Pb, ^{207}Pb/^{204}Pb, and ^{208}Pb/^{204}Pb, based on repeated analyses of standard NBS-981. Measured values for the Pb NBS-981 standard were 36.507 ± 0.012 for ^{208}Pb/^{204}Pb, 15.430 ± 0.004 for ^{207}Pb/^{204}Pb, and 16.891 ± 0.003 for ^{206}Pb/^{204}Pb. Trace element concentrations were measured on cleaned glass chips with a PQ2 inductively coupled mass spectrometer. For more detailed descriptions of the trace element and isotope analytical methods, see (*32*–*34*).
8. D. McKenzie, *Earth Planet. Sci. Lett.* **72**, 149 (1985).
9. M. Spiegelman, T. Elliott, *Earth Planet. Sci. Lett.* **118**, 1 (1993).
10. C. C. Lundstrom, J. Gill, Q. Williams, M. R. Perfit, *Science* **270**, 1958 (1995).
11. H. Zou, A. Zindler, *Geochim. Cosmochim. Acta* **64**, 1809 (2000).
12. R. Batiza *et al*., *Geophys. Res. Lett.* **23**, 221 (1996).
13. Supplementary data on major and trace element concentrations are available on *Science* Online at www.sciencemag.org/cgi/content/full/295/5552/107/DC1.
14. S. J. Goldstein, M. T. Murrell, R. W. Williams, *Earth Planet. Sci. Lett.* **115**, 151 (1993).
15. B. Bourdon, A. Zindler, T. Elliott, C. H. Langmuir, *Nature* **384**, 231 (1996).
16. *D* depends on the mineralogy of the source rock and is given by

$$D = \sum_{1}^{n} x_i K_i$$

where x_i is the mass fraction of mineral *i* in the solid source, K_i is the mineral/melt partition coefficient of mineral *i*, and *n* is the total number of minerals.
17. P. Beattie, *Nature* **363**, 63 (1993).
18. M. M. Hirschmann, E. M. Stolper, *Contrib. Mineral. Petrol.* **124**, 185 (1996).
19. V. J. M. Salters, J. Longhi, *Earth Planet. Sci. Lett.* **166**, 15 (1999).
20. B. J. Wood, J. D. Blundy, J. A. C. Robinson, *Geochim. Cosmochim. Acta* **63**, 1613 (1999).
21. T. Z. LaTourrette, D. S. Burnett, *Earth Planet. Sci. Lett.* **110**, 227 (1992).
22. P. Beattie, *Earth Planet. Sci. Lett.* **117**, 379 (1993).
23. E. H. Hauri, T. P. Wagner, T. L. Grove, *Chem. Geol.* **117**, 149 (1994).
24. The LREE-enriched patterns in PH10-2 and PH34-1 may result from melting of a garnet peridotite source or an LREE-enriched spinel peridotite source. Their (^{230}Th/^{238}U) ratios of smaller than unity argue against the presence of garnet in the source. Low (^{230}Th/^{238}U) ratios of 0.85 to 0.90 can be modeled by dynamic partial melting of a spinel peridotite source when the porosity of the melting zone is 0.2%, the rate of melting is 1.0×10^{-4} kg m^{-3} year^{-1}, D_U = 0.0019, and D_{Th} = 0.0028 [see figure 2, A and D, in (*11*) for details].
25. R. A. Duncan, L. G. Hogan, *Geophys. Res. Lett.* **21**, 1927 (1994).
26. Y. Fialko, *Earth Planet. Sci. Lett.* **190**, 31 (2001).
27. The transport time for subsurface lateral movement (*t*) is given by the following relation:

$$t = -\frac{1}{\lambda_{230}} \ln \frac{(^{230}\mathrm{Th}/^{238}\mathrm{U}) - 1}{(^{230}\mathrm{Th}/^{238}\mathrm{U})_0 - 1}$$

where (^{230}Th/^{238}U) and (^{230}Th/^{238}U)$_0$ are the measured activity ratio in an off-axis sample and the activity ratio of the melt at the start of subsurface lateral transport, respectively. Dividing the distance from the axis (*d*) by *t* yields the average lateral velocity (*v*) of the melt that generated basalts PH8-1 and PH33-3: $v = d/t$. The lateral velocity of 19 to 21 cm year^{-1} is obtained by using (^{230}Th/^{238}U)$_0$ = 1.233. *v* increases when (^{230}Th/^{238}U)$_0$ decreases.
28. A. W. Hofmann, *Earth Planet. Sci. Lett.* **90**, 297 (1988).
29. S. S. Sun, W. F. McDonough, in *Magmatism in the Ocean Basins,* A. D. Saunders, M. J. Norry, Eds. (Geological Society Special Publication, London, 1989), vol. 42, pp. 313–345.
30. A. W. Hofmann, W. M. White, *Earth Planet. Sci. Lett.* **57**, 421 (1982).
31. B. L. Cousens, in *Earth Processes: Reading the Isotopic Code*, A. R. Basu, S. R. Hart, Eds. (American Geophysical Union, Washington, DC, 1996), vol. 95, pp. 207–231.
32. Y. Niu, R. Batiza, *Earth Planet. Sci. Lett.* **148**, 471 (1997).
33. J. G. England *et al*., *Int. J. Mass Spectrom. Ion Processes* **121**, 201 (1992).
34. B. Bourdon, thesis, Columbia University, New York (1994).
35. M. R. Perfit *et al*., *Geology* **22**, 375 (1994).

36. We thank R. Batiza for the samples; A. Sachi for chemistry; two referees for constructive reviews; and M. Reid, V. Salters, R. Odom, D. Loper, A. Stracke, and J. Simon for discussions and help. Supported by NSF grant EAR-9628083 (A.Z.) and NSF postdoctoral fellowship EAR-9805687 (H.Z.).

11 July 2001; accepted 13 November 2001

Formation of Recent Martian Debris Flows by Melting of Near-Surface Ground Ice at High Obliquity

F. Costard,[1] F. Forget,[2]* N. Mangold,[1] J. P. Peulvast[1]

The observation of small gullies associated with recent surface runoff on Mars has renewed the question of liquid water stability at the surface of Mars. The gullies could be formed by groundwater seepage from underground aquifers; however, observations of gullies originating from isolated peaks and dune crests question this scenario. We show that these landforms may result from the melting of water ice in the top few meters of the martian subsurface at high obliquity. Our conclusions are based on the analogy between the martian gullies and terrestrial debris flows observed in Greenland and numerical simulations that show that above-freezing temperatures can occur at high obliquities in the near surface of Mars, and that such temperatures are only predicted at latitudes and for slope orientations corresponding to where the gullies have been observed on Mars.

The observation of small gullies on Mars was one of the more unexpected discoveries of the Mars Observer Camera (MOC) aboard the Mars Global Surveyor spacecraft (*1*). The characteristics of these landforms suggest the local occurrence of a fluid emanating from alcoves located mostly in the upper part of poleward-facing slopes at mid- and high latitudes. Thick accumulations of debris cover the bases of escarpments, whereas the upper parts of the walls have generally steep slopes that are dissected by funnels (Fig. 1A). Malin and Edgett (*1*) convincingly argued that the gullies were probably created by debris flows composed of liquid H_2O mixed with rocks and residual water ice [alternative scenarios include speculations about liquid CO_2 breakout (*2*) and saline groundwater or brine (*3*)]. The lack of fresh impact craters and dust deposits suggest that the gullies are among

[1]UMR8616, Centre National de la Recherche Scientifique (CNRS), OrsayTerre, Équipe de Géomorphologie Planétaire, Université Paris-Sud, 91405, Orsay Cedex, France. [2]Laboratoire de Météorologie Dynamique, CNRS, Université Paris 6, Boîte Postal 99, 75252 Paris 05, France.

*To whom correspondence should be addressed. E-mail: forget@lmd.jussieu.fr